JACS
JOURNAL OF THE AMERICAN CHEMICAL SOCIETY
Article
Cite This: J. Am. Chem. Soc. 2018, 140, 4736−4742
pubs.acs.org/JACS

Carbon Capture by Metal Oxides: Unleashing the Potential of the (111) Facet

Greg A. Mutch,[*,†,‡] Sarah Shulda,[§] Alan J. McCue,[‡] Martin J. Menart,[§] Cristian V. Ciobanu,[∥] Chilan Ngo,[§] James A. Anderson,[‡] Ryan M. Richards,[§] and David Vega-Maza[‡]

[†]School of Engineering, Newcastle University, Newcastle upon Tyne NE1 7RU, United Kingdom
[‡]School of Engineering, University of Aberdeen, Aberdeen AB24 3FX, United Kingdom
[§]Department of Chemistry and Geochemistry, Colorado School of Mines, Golden, Colorado 80401,United States
[∥]Department of Mechanical Engineering and Materials Science Program, Colorado School of Mines, Golden, Colorado 80401, United States

Supporting Information

ABSTRACT: Solid metal oxides for carbon capture exhibit reduced adsorption capacity following high-temperature exposure, due to surface area reduction by sintering. Furthermore, only low-coordinate corner/edge sites on the thermodynamically stable (100) facet display favorable binding toward CO_2, providing inherently low capacity. The (111) facet, however, exhibits a high concentration of low-coordinate sites. In this work, MgO(111) nanosheets displayed high capacity for CO_2, as well as a ∼65% increase in capacity despite a ∼30% reduction in surface area following sintering (0.77 mmol g^{-1} @ 227 m^2 g^{-1} vs 1.28 mmol g^{-1} @ 154 m^2 g^{-1}). These results, unique to MgO(111), suggest intrinsic differences in the effects of sintering on basic site retention. Spectroscopic and computational investigations provided a new structure−activity insight: the importance of high-temperature activation to unleash the capacity of the polar (111) facet of MgO. In summary, we present the first example of a faceted sorbent for carbon capture and challenge the assumption that sintering is necessarily a negative process; here we leverage high-temperature conditions for facet-dependent surface activation.

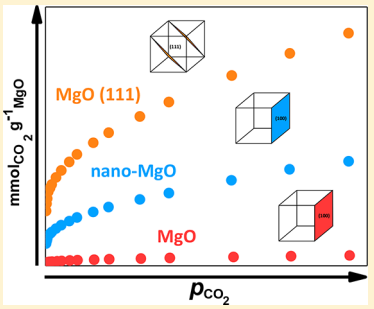

1. INTRODUCTION

Carbon capture, utilization, and storage (CCUS) is a portfolio of processes to combat anthropogenic climate change.[1] Capture is most economically viable for slowing CO_2 release at point sources, e.g., combustion power generation plants. Direct air capture is increasingly discussed,[2−4] to immediately reduce atmospheric CO_2 concentration. CCUS allows the continued use of fossil fuels, or results in net negative carbon emissions, when in combination with bioenergy.[5,6] Utilization refers to the subsequent use of CO_2 in the synthesis of chemicals or enhanced oil recovery, in order to add value.[7,8] Storage is generally the disposal of captured CO_2 in geological formations.[9]

Regardless of the fate of CO_2, it remains the case that capture is the most costly stage of CCUS,[10] due to the immense volumes to be handled. Cyclic absorption−desorption of CO_2 using aqueous amines is inefficient and expensive, generating significant interest in developing new "task-specific" materials as replacements.[11−13] Solid adsorption−desorption cycles, looping processes, offer many advantages over amine scrubbing. They can be distinguished chiefly by their role: the supply of O_2 from air for combustion (providing inherent carbon capture),[14] *in situ* CO_2 sorption during H_2 production,[15] and the removal of CO_2 from flue gases.[16] Solid oxide adsorbents used in these processes, e.g., CaO or MgO, experience particularly harsh environments. They are fluidized, handled at high temperature, and repeatedly cycled between oxidation/reduction or carbonation/calcination reactors. Sintering dramatically reduces sorbent performance, acutely evident in high-temperature CO_2 adsorbents,[17] leading to creative synthetic efforts in producing sintering-resistant materials.[18−20]

For any adsorbent, the initial gas−solid reaction/interaction must occur at the surface. Using the carbonation of CaO in calcium looping as a pertinent example, carbonates first form at the surface, subsequently migrating to the bulk.[21] The capacity of sorbents proposed for low-temperature carbon capture is entirely limited to surface interaction, resulting in a race to produce ever-increasing surface areas—exemplified by metal−organic frameworks (MOFs).[22,23] This approach is likely to fail for solid oxides such as CaO or MgO due to sintering over large numbers of high-temperature cycles. Increased surface area has been shown to enhance capacity, only in a limited number of cycles.[24−26] Considered far less often for CO_2 adsorbents, if at all, is the synthetic control and subsequent utilization of exposed "favorable" crystalline facets. This is surprising considering entire fields (e.g., catalysis) have developed largely by controlling this aspect of solids.[27−30]

In an attempt to bridge this concept with carbon capture, we considered that prominent high-temperature adsorbents

Received: February 19, 2018
Published: March 19, 2018

DOI: 10.1021/jacs.8b01845
J. Am. Chem. Soc. 2018, 140, 4736−4742

include isometric crystals of the rock-salt structure (space group *Fm*3*m*), more specifically group 2 alkaline earth metal oxides, e.g., MgO. In this structure, Mg and O atoms occupy octahedral geometry, forming independent face-centered cubic lattices, which merge together to produce an alternating cation/anion pattern propagating in three dimensions. The thermodynamically favored (100) facet can easily be envisioned as an atomic checkerboard pattern. The (111) facet can be visualized as alternating polar layers of cations and anions (Figure 1a), with

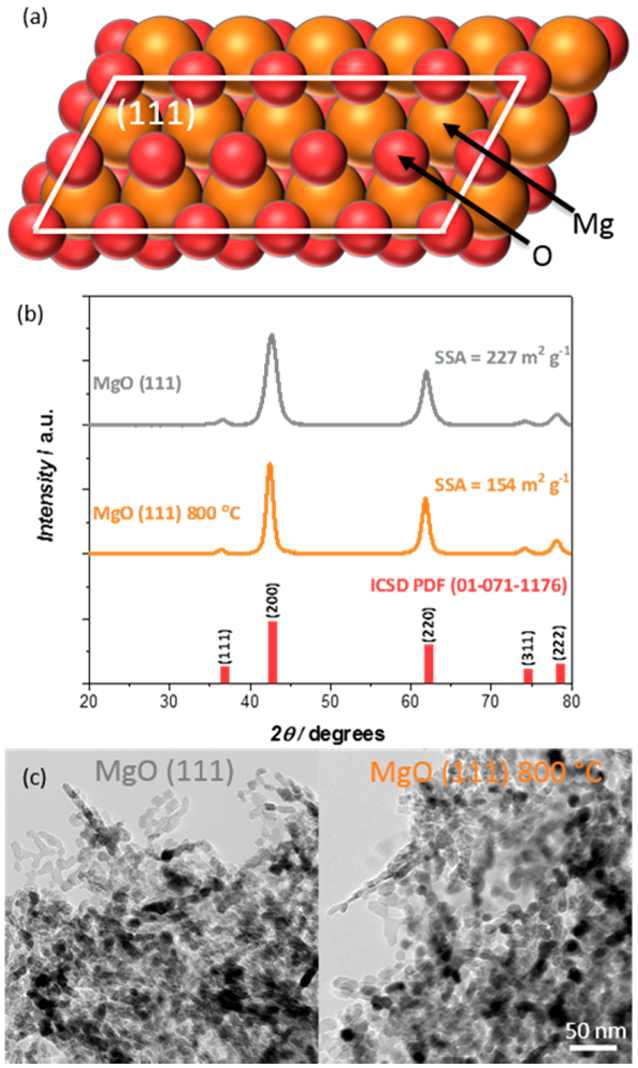

Figure 1. Structure and morphology of MgO(111) nanosheets: (a) top view configuration of a 6×3 O-terminated MgO(111) surface; (b) phase identification by XRD for MgO(111) and MgO(111) 800 °C with specific surface area inset; (c) BF-TEM images of MgO(111) and MgO(111) 800 °C.

surface termination dependent on the environment. In O-rich conditions the facet will be oxygen terminated.[31] The polar (111) facet has been shown to be stable at the nanoscale[32,33] or when hydroxylated.[34−36] *Ab initio* calculations have shown that hydroxylated (111) surfaces are more stable than clean (100) surfaces,[37] with experimental and theoretical investigation providing a hydroxylated surface energy hierarchy of $\gamma_{(111)} < \gamma_{(100)} < \gamma_{(110)}$.[38]

Returning to carbon capture, CO_2 adsorption on metal oxides is largely facilitated by low-coordination O^{2-} sites;[39−42] the acidic CO_2 molecule reacts with a basic O^{2-} site. On predominant MgO (100) facets, CO_2 adsorption will not occur,[42,43] instead favoring corner and edge sites. DFT calculations have shown that the (111) facet of CaO is responsible for carbonate nucleation.[44] Synthesis methods[30,45−47] and examples of catalytic application are present in the literature for (111) metal oxides.[34,48,49] Considering favorable surface chemistry, we postulated that a (111) faceted adsorbent would be promising for carbon capture. Such a sorbent should possess (1) enhanced reactivity toward CO_2 (increased basicity of the polar O^{2-} sites), (2) enhanced capacity for CO_2 (doubled population of exposed O^{2-} compared to a (100) facet), and (3) unique CO_2 adsorption phenomena related to the (111) facet following high-temperature treatment (removal of the stabilizing hydroxylated surface layer to expose O^{2-}).

Herein, we show that at sintering conditions found in practical application (800 °C), MgO(111) nanosheets experience a ∼30% reduction in surface area due to sintering, yet provide a ∼65% increase in CO_2 capacity (0.77 mmol g^{-1} @ 227 m^2 g^{-1} vs 1.28 mmol g^{-1} @ 154 m^2 g^{-1}). We compare MgO(111) nanosheets with commercial MgO, conventionally prepared nanoparticle MgO (nano-MgO), and MgO(111) treated at 800 °C to unambiguously attribute the enhanced capacity to the presence of the cleaned (111) facet. Furthermore, we show experimentally and theoretically that the high-temperature treatment removes specific surface hydroxyl groups, providing insight into a new structure−activity relationship leading to enhanced capacity. The article is structured in four parts: (1) the impact of high-temperature treatment on the physical properties of MgO(111), (2) the subsequent paradoxical effect on CO_2 adsorption capacity, (3) the surface chemistry changes facilitating the enhanced capacity, and (4) implications for carbon capture. Throughout, MgO(111) refers to the as-prepared sample pretreated at 400 °C (below the temperature of calcination during synthesis) and MgO(111) 800 °C refers to the as-prepared sample pretreated at 800 °C.

2. RESULTS

2.1. Adsorbent Characterization. MgO(111) and MgO(111) 800 °C were identified as periclase MgO in the Inorganic Crystal Structure Database (ICSD PDF 01-071-1176) (Figure 1b). Sharpening of the MgO(111) 800 °C diffractogram indicated crystallite size growth (Scherrer average crystallite size increase from 5.3 to 8.5 nm). Bright-field transmission electron microscopy (BF-TEM) showed that MgO(111) was composed of plate-like nanosheets within a size range of 5−25 nm (Figure 1c). After treatment at 800 °C *in vacuo* for 2 h, morphology remained consistent, with growth of nanosheet size range to 15−30 nm (Figure 1c).

Scanning transmission electron microscopy (STEM) imaging and energy-dispersive spectroscopy (EDS) further showed that both morphology and compositional homogeneity remained consistent after heat treatment (Figure S1). Nitrogen adsorption−desorption confirmed the morphology observation, with H3 hysteresis loops present in all Type IV isotherms, indicative of aggregates of plate-like crystallites with intraparticle mesoporosity (Figure S2a).[50] The major effect of treatment at 800 °C was a ∼30% reduction in surface area from 227 to 154 m^2 g^{-1}, with little impact on the mesoporous pore size distribution (Figures 1b and S2). Taken together, the diffraction, microscopy, and N_2 adsorption−desorption clearly

DOI: 10.1021/jacs.8b01845
J. Am. Chem. Soc. 2018, 140, 4736−4742

evidenced a degree of sintering in MgO(111) after treatment at 800 °C.

2.2. Sintering and CO_2 Adsorption Capacity. It is generally recognized that sintering of an adsorbent material results in reduction of adsorption capacity, in terms of saturated gas uptake. Examples include linear correlations between H_2 gravimetric density and surface area of carbon aerogels,[51] as well as CO_2 uptake and surface area of MOFs and carbons.[52,53] One would therefore expect a significant reduction in the CO_2 capacity of the sintered MgO 800 °C nanosheets, considering the ~30% reduction in surface area from 227 to 154 $m^2\ g^{-1}$ (Figure S2a). However, a ~65% increase in CO_2 adsorption capacity was observed (Figure 2), from 0.77 to 1.28 mmol g^{-1},

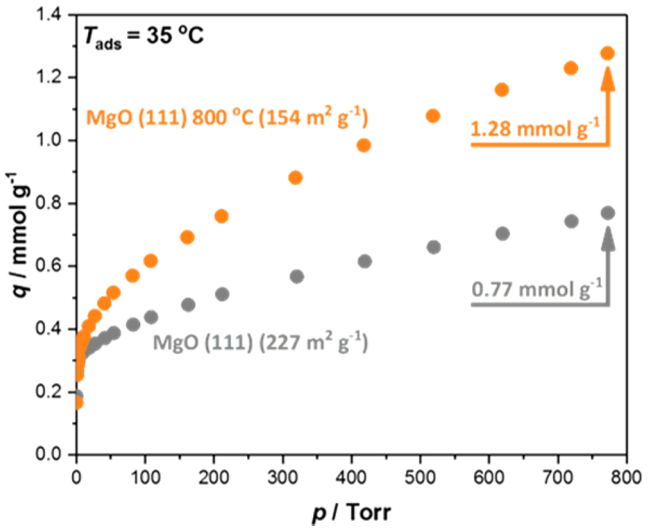

Figure 2. CO_2 adsorption isotherms (T_{ads} = 35 °C) on MgO(111) and MgO(111) 800 °C with specific surface areas inset. Lower surface area conversely provides higher CO_2 uptake.

indicating increased utility of the surface capacity of MgO. It is prudent to point out that carbonate formation on MgO is largely limited to the surface, particularly at low temperature (T_{ads} = 35 °C).[54,55] Commercial MgO (SSA = 7 $m^2\ g^{-1}$) and conventionally prepared nano-MgO (SSA = 84 $m^2\ g^{-1}$) (Figure S2b) were compared with MgO(111) to investigate the link between increased capacity and presence of the (111) facet (Figure S3c,d). MgO(111) 800 °C gave the highest adsorption capacity of all samples (Figure S3b), 2 orders of magnitude higher than commercial MgO. A simple explanation of increased physisorption to explain the increased capacity of MgO(111) after sintering is not possible due to the reduction in surface area. The full set of isotherms for all samples are provided, including adsorption at elevated temperature (T_{ads} = 35–400 °C) (Figure S3).

2.3. Surface Chemistry and Structure–Activity Relationship. Considering the paradoxical impact of sintering MgO(111) on CO_2 adsorption capacity, the surface chemistry of MgO(111) was investigated before and after sintering. Diffuse-reflectance infrared spectroscopy (DRIFTS) evidenced two "free" surface hydroxyl vibrational modes at 3760 and 3723 cm^{-1} among a range of hydrogen-bonded hydroxyl groups (ca. 3650–3300 cm^{-1}) (Figure 3a).[56,57] Following treatment at 800 °C *in vacuo* for 2 h, a slight reduction in intensity of the band at 3760 was apparent, with the mode at 3723 cm^{-1} significantly reduced in intensity. Surface dehydration of the O-terminated (111) surface would leave behind the necessary low-coordinate O^{2-} sites required for CO_2 adsorption, as well as Mg^{2+} exposed by O vacancies.

Density functional theory (DFT) calculations were performed to elucidate the nature of the experimentally observed peaks at 3760 and 3723 cm^{-1}. A range of adsorbates were investigated, water and H (of the OH group), on O- and Mg-terminated MgO(111) surfaces, with a selection of surface coverage variations (Figure S4). A 100% H-covered O-terminated surface gave a calculated OH stretch mode frequency of 3764 cm^{-1}, sufficiently close to the experimental value so as to confirm the 3760 cm^{-1} band belonged to an OH stretching mode on such a surface (Figure 3a). A 100% H-covered O-terminated surface has been shown computationally and experimentally to be extremely stable.[58,59] Other simulated (111) surfaces (Figure S4a–d), as well as a small selection of MgO (110) and MgO (100) surfaces (not shown), could not be assigned to the remaining 3723 cm^{-1} band as a result of large frequency mismatch. These large differences were due to significant structural modifications such as the presence of water, or bonding to Mg^{2+} sites in place of O^{2-} sites. However, modifying the 100% H-covered O-terminated surface to remove every second row of OH groups, i.e. 50% H-covered O-terminated surface (Figure S4e), gave a frequency band between 3733 and 3725 cm^{-1}. This indicated that the 3723 cm^{-1} band was likely due to portions of the O-terminated surface not 100% covered with hydrogen (Figure 3a). Sintering at 800 °C removed hydrogen to reveal O^{2-} sites suitable for CO_2 adsorption, likely via condensation which would also reveal subsurface Mg^{2+}. Considered together with the DFT calculations (Figure S4), the major surface activation was the removal of hydroxyl groups from a partially covered (111) surface (3723 cm^{-1}). This would be logical considering the stability of the fully hydroxylated O-terminated surface.[58,59] A more intricate dependence of the OH stretch mode frequency on H-coverage may well exist, with alternative explanations including hydrogen bonding of the 3760 cm^{-1} hydroxyl and lower index defects and edge planes.[60] The loss of the 3723 cm^{-1} peak indicated that it was strongly involved in changes to the surface upon sintering.

Further evidence for the creation of new basic O^{2-} sites on the (111) surface after treatment at 800 °C was provided by temperature-programmed desorption of CO_2 (CO_2-TPD) (Figure 3b). Briefly, MgO(111) was treated in flowing He at 400 and 800 °C for 2 h before exposure to CO_2 and subsequent TPD. During temperature ramping from 50 to 400 °C, CO_2 was evolved in a similar manner for both 400 and 800 °C treated samples (Figure 3b). Weak (T_d < 120 °C) and strong (T_d > 275 °C) basic site densities were similar after both treatments (Table S1). In the intermediate strength range (T_d = 120–275 °C) a ~30% increase was observed after treatment at 800 °C, due to the removal of hydroxyl functionality evidenced previously (Figure 3a). MgO(111) will present a large population of intermediate basicity sites, due to the unique structure;[61] treating at high-temperature increases this population further. Hydroxyl functionality on MgO powders has previously been shown to be stable to 500 °C.[56,57] Therefore, sintering at 800 °C explores a new temperature region and results in the removal of further hydroxyl functionality, creating further sites for CO_2 adsorption. After sintering, the total number of basic sites increased from 357 to 415 $\mu mol\ g^{-1}$ assuming a stoichiometry of one basic site per CO_2 molecule. As will be shown later, this assumption gives a

DOI: 10.1021/jacs.8b01845
J. Am. Chem. Soc. 2018, 140, 4736–4742

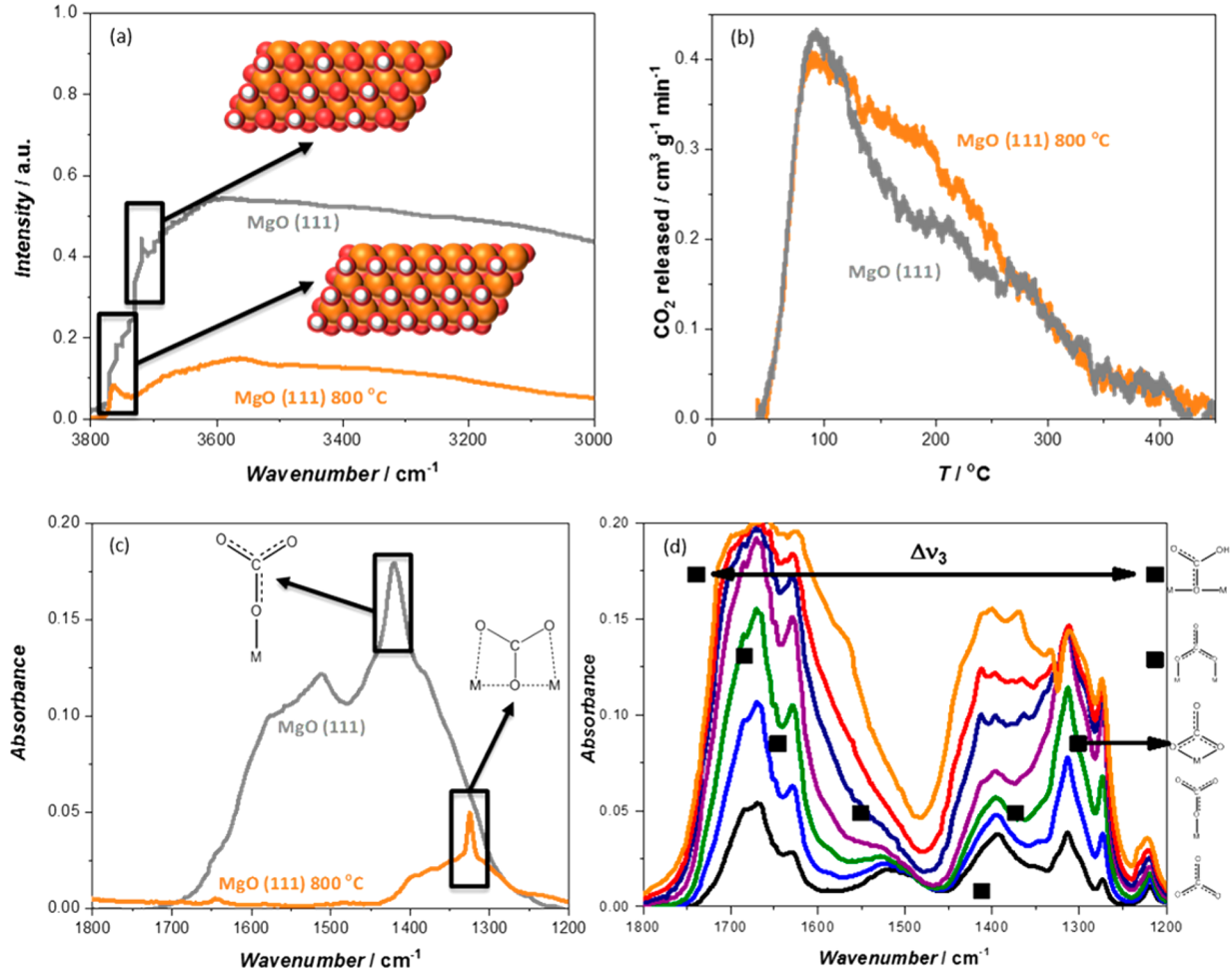

Figure 3. Surface chemistry investigation of MgO(111). (a) DRIFTS spectra of MgO(111) and MgO(111) 800 °C evidencing surface hydroxyl removal; DFT-simulated surfaces inset used to calculate hydroxyl stretch frequencies (Figure S4). (b) CO_2-TPD of MgO(111) and MgO(111) 800 °C evidencing creation of new intermediate basicity sites due to surface hydroxyl removal. (c) *In situ* transmission FTIR spectra of MgO(111) and MgO(111) 800 °C of residual carbonates following thermal pretreatment. (d) *In situ* transmission FTIR spectra of MgO(111) 800 °C following exposure of increasing pressures of CO_2, with band growth in the 1800−1200 cm^{-1} region evidencing formation of a variety of carbonates. Right side axis displays different carbonate structures assignable on the basis of asymmetric stretching mode (ν_3) splitting.

relative indication of basic site density, with any true evaluation dependent on carbonate coordination—far from trivial on MgO(111) (Figure 3d). Total CO_2 uptake closely matched that of the equilibrated isotherm at the CO_2 partial pressure used during TPD dosing (ca. 65 Torr).

Regarding the presence and formation of carbonates on the MgO(111) surface, significant differences following 2 h treatment at 400 and 800 °C *in vacuo* were observed by *in situ* transmission FTIR spectroscopy (Figure 3c,d). Absorption bands due to carbonate species were observed in the 1800−1200 cm^{-1} region following both treatments, yet the intensity decrease in the carbonate region was more pronounced following 800 °C treatment (Figure 3c). A simple argument for increased capacity would be that removal of more carbonate species at 800 °C provides additional capacity for CO_2. However, as surface area was reduced by ∼30% yet capacity increased by ∼65%, a further explanation is required, i.e., the aforementioned creation of O^{2-} and Mg^{2+} sites following sintering (Figure 3a). After treatment at 400 °C, a prominent feature at 1420 cm^{-1} indicated the presence of monodentate carbonates on the (111) surface.[62] A maximum at 1512 cm^{-1} and weaker features/shoulders at 1650, 1590, and 1380 cm^{-1} indicated that a range of carbonate species remained on the surface.[63] These features were further evidence of the presence of the (111) surface contributing to CO_2 adsorption, as on well-defined (100) facets, absorption in the 1600−1350 cm^{-1} range was not observed.[64] Following treatment at 800 °C, a uniquely sharp feature at 1325 cm^{-1} and a weak feature at 1645 cm^{-1} were assigned as tridentate carbonate species on the (111) surface facilitated by surface defects, either O^{2-} vacancies to expose subsurface Mg^{2+}, or at edges.[62] Weak absorption at 1580 and 1400−1300 cm^{-1} indicated the presence of bidentate and monodentate carbonates.[63] Upon exposure of CO_2 to MgO(111) after treatment at 800 °C, a range of carbonate species were formed, identifiable on the basis of the splitting of the ν_3 asymmetric stretching mode (Figure 3d).[63] A variety of monodentate and bidentate carbonate species were identified, as well as bicarbonates formed in the presence of remaining surface hydroxyl groups, as we have observed previously in related systems.[65,66] In agreement with decreasing CO_2 capacity at increased temperature observed in CO_2 adsorption isotherms (Figure S3), an absorption maximum at 2345 cm^{-1} indicative of physisorbed CO_2 was present throughout (not shown). The complexity of carbonate speciation highlights the convoluted nature of the CO_2-TPD basic site quantification; i.e., assuming

DOI: 10.1021/jacs.8b01845
J. Am. Chem. Soc. 2018, 140, 4736−4742

a stoichiometry of one binding site per CO_2 molecule is incorrect.

2.4. Impact of the (111) Facet in Carbon Capture Processes. Clearly, the expected impact of surface area reduction on surface adsorption capacity is more complex than a simple linear relationship. The presence of the (111) facet overcame the significant reduction in surface area, facilitated by the removal of specific hydroxyl groups from the surface; wider impacts of these findings are briefly discussed. First, in calcium looping, rehydration is a common strategy to enhance sorbent utility.[16] Steam hydration of CaO (as opposed to hydration of $CaCO_3$) is favored for regenerating spent sorbent.[67] Current interpretations of the positive impact of hydration involve the creation of new surface area and porosity, through rupturing of CaO particles upon hydration due to the larger specific volume of $Ca(OH)_2$. Consider that hydration stabilizes the (111) facet of rock salt oxides,[34−36] and that this hydrated sorbent enters a high-temperature carbonating reactor. Taken with our findings, we suggest that faceting plays a unique role in enabling the formation and retention of highly active CO_2 adsorption sites during hydration, despite overall loss of surface area. Furthermore, it is worth noting that so-called "double salt" carbon capture sorbents (a metal oxide with molten salt on the surface),[68−70] and dual-phase molten salt−ceramic membranes,[71] may inadvertently experience faceting effects similar to those noted here. Strong electrostatic interactions between molten salt ions and solid metal oxide surfaces significantly lower the surface energy of polar facets.[45] As a result, polar faceting in these sorbents and devices may well occur, contributing to interfacial phenomena.

3. CONCLUSIONS

An approach routinely applied in catalysis—synthetic control over crystalline facets—produced a sorbent for carbon capture with high capacity. This activity was due to the preferential exposure of the polar (111) facet and the surface exposed after thermal treatment. MgO(111) nanosheets displayed a ∼65% increase in CO_2 adsorption capacity following sintering at 800 °C. This was unexpected as the treatment also resulted in a ∼30% reduction in surface area. Further interrogation through spectroscopy and theory demonstrated that removal of hydroxyl functionality from the (111) facet exposes and retains low-coordinate O^{2-} and Mg^{2+} sites, facilitating enhanced capacity.

Of consideration for all carbon capture processes, is the cost of sorbent manufacture. Although our synthesized (111) sorbent shows promising capacity, we suggest that the most important practical conclusion is that the addition of steam in looping cycles to stabilize the (111) facet and subsequent high-temperature activation may well enhance capacity in existing affordable adsorbents. To be clear, we wish to highlight that control of specific facets through activation procedures easily integrated with existing pilot-scale carbon capture processes (e.g., calcium looping) is of primary significance.

In summary, we challenge the assumption that sintering is necessarily a negative process in high-temperature looping cycles for CO_2 adsorption; the high-temperature conditions can be leveraged for facet-dependent surface activation. In this case, we have shown that the presence of specific facets can be more important than the total surface area lost during sintering. We provide the first example of a faceted sorbent (of specified morphology) for carbon capture and give insight into new structure−activity relationships in materials relevant for environmental processes.

4. MATERIALS AND METHODS

4.1. Adsorbent Synthesis. MgO(111) nanosheets were prepared following a modified aero-gel methodology.[46] Magnesium belt (Mg) (Sigma-Aldrich, 99.5%) was roughened with sandpaper and cleaned with acetone (Pharmco-Aaper, 99.5%). The roughened magnesium was cut into small portions and dissolved in anhydrous methanol (Avantor, 99.9%) under nitrogen (Praxair, >99.5%). Once dissolved, 4-methoxyl-benzyl alcohol (BZ) (Sigma-Aldrich, 98%) was added (molar ratio 2:1, Mg:BZ) and stirred for 5 h. Water in methanol was added (molar ratio 2:1, H_2O:Mg, 30.0 mL of MeOH) dropwise with stirring. After 12 h of stirring the mixture was transferred to an autoclave, purged, and then pressurized to 10 bar with argon (Praxair, >99.998%). The mixture was heated at 265 °C for 15 h, followed by venting of the supercritical solvent. The collected powder was calcined at 500 °C in air for 6 h. Commercial MgO (Sigma-Aldrich, 98%) and conventionally prepared nano-MgO (NanoScale Corporation, NanoActive MgO ≥95%) were used as received.

4.2. Adsorbent Characterization. Surface area and porosity analyses were conducted using a Micromeritics Tristar with N_2 as adsorbate. Powdered samples were treated at 200 °C for 3 h in flowing N_2. Adsorption−desorption was performed at −196 °C, with the Brunauer−Emmett−Teller (BET) method applied to determine surface area and the Barrett−Joyner−Halenda (BJH) method used to determine pore volume and pore size distribution.

X-ray diffraction (XRD) data were collected with an Empyrean diffractometer (PANalytical, NL) using Cu Kα radiation (λ = 1.54 Å). Powdered samples (ca. 0.2 g) were supported in aluminum holders after loose packing. Patterns were collected from 10 to 80° 2θ with a step size of 0.026° and a total collection time of 20 min. Scherrer crystallite size analysis was performed on the (200) MgO periclase peak.

Transmission electron microscopy (TEM) characterization was conducted using an FEI Co. Talos F200X with a FEI X-FEG high-brightness electron source operating at an accelerating voltage of 200 kV. Samples were prepared as an ultrasonic suspension in ethanol spread on a carbon-coated copper grid. Bright-field (BF-TEM), scanning (STEM), and energy dispersive spectroscopy (EDS) modes were utilized.

4.3. CO_2 Adsorption. CO_2 adsorption isotherms were measured with a Micromeritics ASAP 2020C. Powdered samples were loaded into a quartz tube, surrounded by loosely packed plugs of quartz wool. Manual and automatic leak checks were conducted upon sample loading and immediately before adsorption isotherm collection, respectively. CO_2 (BOC, 99.8%) was connected to the apparatus through a moisture trap (Alltech Hydro-Purge) filled with freshly conditioned adsorbent (Molecular Sieve 3A, Fischer Scientific). Sequenced experiments were run to obtain isotherms at 35, 100, 200, 300, and 400 °C with initial and intermittent 400 and 800 °C high-temperature treatments (i.e., below and above the calcination temperature of synthesized sorbents).

4.4. Surface Chemistry and Structure−Activity Relationship. Diffuse reflectance infrared spectroscopy (DRIFTS) was conducted using a Thermo Nicolet 4700 IR spectrometer fitted with a liquid nitrogen cooled detector and DRIFTS accessory. KBr under vacuum ($<3 \times 10^{-2}$ Torr) at room temperature was used as a background for all spectra. MgO(111) was heated to 400 °C, held for 15 min, and then heated to 800 °C and held for 2 h. All ramp rates were 10 °C min^{-1}. The sample was then cooled to room temperature before spectral acquisition. The complete procedure was under vacuum. Spectra were collected as an accumulation of 120 scans over a range of 4000−600 cm^{-1} at a resolution of 4 cm^{-1}.

CO_2 temperature-programmed desorption (CO_2-TPD) was performed in a Micromeritics AutoChem II 2920 chemisorption instrument. Samples were treated *in situ* with a 10 °C min^{-1} ramp under flowing He (UHP, 99.999%) to a final temperature of 400 or 800 °C and held for 2 h before being cooled to 40 °C under flowing

DOI: 10.1021/jacs.8b01845
J. Am. Chem. Soc. 2018, 140, 4736−4742

He. The samples were dosed with a 10% CO_2/He blend for 1.5 h and then purged with He for 1 h to remove physisorbed CO_2. The thermal desorption of chemisorbed CO_2 was then performed in flowing He at a ramp rate of 10 °C min^{-1} to a final temperature of 800 °C while the evolved CO_2 was quantified by changes in downstream thermal conductivity. Blank He-TPD experiments were performed on both samples to remove baseline differences between pretreatment temperatures due to desorbing water. All flow rates were 50 mL min^{-1}. Sample basicities are reported on a dry sample mass basis with an assumed stoichiometry of one basic site per CO_2 molecule (the appropriateness of which is discussed in the manuscript).

In situ Fourier transform infrared spectroscopy (FTIR) was performed using a PerkinElmer Spectrum 100 spectrometer. Powdered samples (ca. 20 mg) were pressed (Specac 15.011 Manual Hydraulic Press) at 1−3 tons into self-supporting discs of 13 mm diameter. Sample discs were suspended in a custom-made quartz holder and loaded into a high-vacuum glass line apparatus, fitted with a high-temperature furnace (T_{max} = 1000 °C). Sample discs were treated at 400 or 800 °C under high vacuum (<3.75 × 10^{-6} Torr) for 2 h. A 23% CO_2 mixture (balance N_2) was used to fill a glass bulb which was attached to the vacuum apparatus. Following high-temperature treatment, samples were cooled to room temperature under high vacuum before exposure to increasing pressures of CO_2. Spectra were collected as an accumulation of 25 scans over a range of 4000−1000 cm^{-1} at a resolution of 4 cm^{-1} with automated atmospheric background subtraction. Experimental spectra were subtracted from the initial spectrum collected immediately following pretreatment. In this way, changes to spectral features are only related to differences in the sample following CO_2 exposure.

DFT calculations were performed using the generalized gradient approximation (GGA) with the revised Perdew−Burke−Ernzerhof[72,73] functional and the plane-waves code VASP.[74,75] Adsorbates on the surface were relaxed via conjugate-gradient in the presence of dipole corrections using a plane-wave cutoff of 500 eV, a 6×3 surface cell, and Monkhorst−Pack *k*-point grid of 3×3×1 for sampling the Brillouin zone. Once residual forces on all ions had decreased below 0.005 eV/Å, relaxations were stopped and frequency calculations were performed. Several adsorbates, water and H (of the OH group), on both O- and Mg-terminated (111) surfaces were tested.

■ ASSOCIATED CONTENT

Supporting Information

The Supporting Information is available free of charge on the ACS Publications website at DOI: 10.1021/jacs.8b01845.

Synthesis procedure, experimental methods, computational methods, transmission microscopy images, N_2 adsorption−desorption isotherms and pore size distributions, additional CO_2 adsorption isotherms, and density functional theory model surfaces, including Figures S1−S4 and Table S1 (PDF)

■ AUTHOR INFORMATION

Corresponding Author

*gregamutch@gmail.com

ORCID

Greg A. Mutch: 0000-0002-7267-3234
Cristian V. Ciobanu: 0000-0002-8476-4467
Chilan Ngo: 0000-0003-4084-098X
James A. Anderson: 0000-0003-0441-7578
Ryan M. Richards: 0000-0001-8792-3964

Notes

The authors declare no competing financial interest.

■ ACKNOWLEDGMENTS

This work was supported by the Engineering and Physical Sciences Research Council (EPSRC) via a Doctoral Training Grant (EP/K0502960/1) and a Doctoral Prize Fellowship (EP/M50791X/1) for G.A.M. Dedicated to the memory of Kenneth J. Klabunde.

■ REFERENCES

(1) Boot-Handford, M. E.; Abanades, J. C.; Anthony, E. J.; Blunt, M. J.; Brandani, S.; Mac Dowell, N.; Fernández, J. R.; Ferrari, M.-C.; Gross, R.; Hallett, J. P.; Haszeldine, R. S.; Heptonstall, P.; Lyngfelt, A.; Makuch, Z.; Mangano, E.; Porter, R. T. J.; Pourkashanian, M.; Rochelle, G. T.; Shah, N.; Yao, J. G.; Fennell, P. S. *Energy Environ. Sci.* **2014**, *7* (1), 130.
(2) Sanz-Pérez, E. S.; Murdock, C. R.; Didas, S. A.; Jones, C. W. *Chem. Rev.* **2016**, *116*, 11840.
(3) Bhatt, P. M.; Belmabkhout, Y.; Cadiau, A.; Adil, K.; Shekhah, O.; Shkurenko, A.; Barbour, L. J.; Eddaoudi, M. *J. Am. Chem. Soc.* **2016**, *138* (29), 9301−9307.
(4) McDonald, T. M.; Lee, W. R.; Mason, J. A.; Wiers, B. M.; Hong, C. S.; Long, J. R. *J. Am. Chem. Soc.* **2012**, *134* (16), 7056−7065.
(5) Zhao, X.; Zhou, H.; Sikarwar, V. S.; Zhao, M.; Park, A.-H. A.; Fennell, P. S.; Shen, L.; Fan, L.-S. *Energy Environ. Sci.* **2017**, *10*, 1885.
(6) Bui, M.; Fajardy, M.; Mac Dowell, N. *Appl. Energy* **2017**, *195*, 289.
(7) Rubin, E. S.; Davison, J. E.; Herzog, H. J. *Int. J. Greenhouse Gas Control* **2015**, *40*, 378.
(8) Abanades, J. C.; Rubin, E. S.; Mazzotti, M.; Herzog, H. J. *Energy Environ. Sci.* **2017**, *10*, 2491−2499.
(9) Benson, S. M.; Cole, D. R. *Elements* **2008**, *4* (5), 325.
(10) Nandi, S.; Collins, S.; Chakraborty, D.; Banerjee, D.; Thallapally, P. K.; Woo, T. K.; Vaidhyanathan, R. *J. Am. Chem. Soc.* **2017**, *139* (5), 1734−1737.
(11) Bates, E. D.; Mayton, R. D.; Ntai, I.; Davis, J. H. *J. Am. Chem. Soc.* **2002**, *124* (6), 926−927.
(12) Kim, T. K.; Lee, K. J.; Cheon, J. Y.; Lee, J. H.; Joo, S. H.; Moon, H. R. *J. Am. Chem. Soc.* **2013**, *135* (24), 8940−8946.
(13) Hicks, J. C.; Drese, J. H.; Fauth, D. J.; Gray, M. L.; Qi, G.; Jones, C. W. *J. Am. Chem. Soc.* **2008**, *130* (10), 2902−2903.
(14) Adanez, J.; Abad, A.; Garcia-Labiano, F.; Gayan, P.; De Diego, L. F. *Prog. Energy Combust. Sci.* **2012**, *38* (2), 215.
(15) Hufton, J. R.; Mayorga, S.; Sircar, S. *AIChE J.* **1999**, *45* (2), 248.
(16) Blamey, J.; Anthony, E. J.; Wang, J.; Fennell, P. S. *Prog. Energy Combust. Sci.* **2010**, *36* (2), 260.
(17) Erans, M.; Manovic, V.; Anthony, E. J. *Appl. Energy* **2016**, *180*, 722.
(18) Zhao, M.; Shi, J.; Zhong, X.; Tian, S.; Blamey, J.; Jiang, J.; Fennell, P. S. *Energy Environ. Sci.* **2014**, *7*, 3291.
(19) Broda, M.; Müller, C. R. *Adv. Mater.* **2012**, *24* (22), 3059.
(20) Liu, W.; Feng, B.; Wu, Y.; Wang, G.; Barry, J.; da Costa, J. C. D. *Environ. Sci. Technol.* **2010**, *44* (8), 3093.
(21) Mutch, G. A.; Anderson, J. A.; Vega-Maza, D. *Appl. Energy* **2017**, *202*, 365.
(22) Farha, O. K.; Eryazici, I.; Jeong, N. C.; Hauser, B. G.; Wilmer, C. E.; Sarjeant, A. a.; Snurr, R. Q.; Nguyen, S. T.; Yazaydin, A. O.; Hupp, J. T. *J. Am. Chem. Soc.* **2012**, *134* (36), 15016.
(23) Farha, O. K.; Yazaydın, A. Ö.; Eryazici, I.; Malliakas, C. D.; Hauser, B. G.; Kanatzidis, M. G.; Nguyen, S. T.; Snurr, R. Q.; Hupp, J. T. *Nat. Chem.* **2010**, *2* (11), 944.
(24) Bian, S.-W.; Baltrusaitis, J.; Galhotra, P.; Grassian, V. H. *J. Mater. Chem.* **2010**, *20* (39), 8705.
(25) Bhagiyalakshmi, M.; Lee, J. Y.; Jang, H. T. *Int. J. Greenhouse Gas Control* **2010**, *4*, 51.
(26) Wang, S.; Yan, S.; Ma, X.; Gong, J. *Energy Environ. Sci.* **2011**, *4* (10), 3805.
(27) Zhou, K.; Li, Y. *Angew. Chem., Int. Ed.* **2012**, *51* (3), 602.
(28) Pal, J.; Pal, T. *Nanoscale* **2015**, *7* (34), 14159.
(29) Huang, W. *Acc. Chem. Res.* **2016**, *49* (3), 520.

DOI: 10.1021/jacs.8b01845
J. Am. Chem. Soc. 2018, 140, 4736−4742

(30) Abdelhamid, A. A.; Yu, Y.; Yang, J.; Ying, J. Y. *Adv. Mater.* **2017**, *29* (32), 1701427.
(31) Finocchi, F.; Barbier, A.; Jupille, J.; Noguera, C. *Phys. Rev. Lett.* **2004**, *92* (13), 136101.
(32) Goniakowski, J.; Finocchi, F.; Noguera, C. *Rep. Prog. Phys.* **2008**, *71* (1), 0-16501.
(33) Noguera, C.; Goniakowski, J. *Chem. Rev.* **2013**, *113* (6), 4073.
(34) Cadigan, C. A.; Corpuz, A. R.; Lin, F.; Caskey, C. M.; Finch, K. B. H.; Wang, X.; Richards, R. M. *Catal. Sci. Technol.* **2013**, *3* (4), 900.
(35) Hacquart, R.; Jupille, J. *Chem. Phys. Lett.* **2007**, *439* (1−3), 91.
(36) Lee, M. H.; et al. *Phys. Rev. B: Condens. Matter Mater. Phys.* **1995**, *52* (15), 10823.
(37) Wander, A.; Bush, I.; Harrison, N. *Phys. Rev. B: Condens. Matter Mater. Phys.* **2003**, *68* (23), 233405.
(38) Geysermans, P.; Finocchi, F.; Goniakowski, J.; Hacquart, R.; Jupille, J. *Phys. Chem. Chem. Phys.* **2009**, *11* (100), 2228.
(39) Pacchioni, G. *Surf. Sci.* **1993**, *281* (1−2), 207.
(40) Meixner, D. L.; Arthur, D. A.; George, S. M. *Surf. Sci.* **1992**, *261*, 141.
(41) Daub, C. D.; Patey, G. N.; Jack, D. B.; Sallabi, A. K. *J. Chem. Phys.* **2006**, *124*, 114706.
(42) Jensen, M. B.; Pettersson, L. G. M.; Swang, O.; Olsbye, U. *J. Phys. Chem. B* **2005**, *109* (35), 16774.
(43) Karlsen, E. J.; Nygren, M. A.; Pettersson, L. G. M. *J. Phys. Chem. B* **2003**, *107* (31), 7795.
(44) Besson, R.; Favergeon, L. *J. Phys. Chem. C* **2013**, *117*, 8813.
(45) Xu, T.; Zhou, X.; Jiang, Z.; Kuang, Q.; Xie, Z.; Zheng, L. *Cryst. Growth Des.* **2009**, *9* (1), 192.
(46) Zhu, K.; Hu, J.; Kübel, C.; Richards, R. *Angew. Chem., Int. Ed.* **2006**, *45* (43), 7277.
(47) Hu, J.; Zhu, K.; Chen, L.; Yang, H.; Li, Z.; Suchopar, A.; Richards, R. *Adv. Mater.* **2008**, *20* (2), 267.
(48) Zhu, K.; Hua, W.; Deng, W.; Richards, R. M. *Eur. J. Inorg. Chem.* **2012**, *2012* (17), 2869.
(49) Hu, J.; Zhu, K.; Chen, L.; Kubel, C.; Richards, R. *J. Phys. Chem. C* **2007**, *111*, 12038.
(50) Sing, K. S. W.; Everett, D. H.; Haul, R. A. W.; Moscou, L.; Pierotti, R. A.; Rouquerol, J.; Siemieniewska, T. *Pure Appl. Chem.* **1985**, *57* (4), 603.
(51) Kabbour, H.; Baumann, T. F.; Satcher, J. H.; Saulnier, A.; Ahn, C. C. *Chem. Mater.* **2006**, *18* (26), 6085.
(52) Li, J.; Ma, Y.; Mccarthy, M. C.; Sculley, J.; Yu, J.; Jeong, H.; Balbuena, P. B.; Zhou, H.-C. *Coord. Chem. Rev.* **2011**, *255* (15−16), 1791.
(53) Wang, L.; Yang, R. T. *J. Phys. Chem. C* **2012**, *116*, 1099.
(54) Gregg, S. J.; Ramsay, J. D. *J. Chem. Soc. A* **1970**, *1* (956), 2784.
(55) Prashar, A. K.; Seo, H.; Choi, W. C.; Kang, N. Y.; Park, S.; Kim, K.; Min, D. Y.; Kim, H. M.; Park, Y.-K. *Energy Fuels* **2016**, *30*, 3298.
(56) Knozinger, E.; Jacob, K.-H.; Singh, S.; Hofmann, P. *Surf. Sci.* **1993**, *290*, 388.
(57) Coluccia, S.; Marchese, L.; Lavagnino, S.; Anpo, M. *Spectrochim. Acta* **1987**, *43A*, 1573.
(58) Ciston, J.; Subramanian, A.; Marks, L. D. *arXiv* **2008**, https://arxiv.org/pdf/0809.2459.
(59) Lazarov, V. K.; Plass, R.; Poon, H.; Saldin, D. K.; Weinert, M.; Chambers, S. A.; Gajdardziska-Josifovska, M. *Phys. Rev. B: Condens. Matter Mater. Phys.* **2005**, *71*, 115434.
(60) Ciston, J.; Subramanian, A.; Marks, L. D. *Phys. Rev. B: Condens. Matter Mater. Phys.* **2009**, *79*, 084521.
(61) Verziu, M.; Cojocaru, B.; Hu, J.; Richards, R.; Ciuculescu, C.; Filip, P.; Parvulescu, V. I. *Green Chem.* **2008**, *10*, 373.
(62) Cornu, D.; Guesmi, H.; Krafft, J.-M.; Lauron-Pernot, H. *J. Phys. Chem. C* **2012**, *116*, 6645.
(63) Busca, G.; Lorenzelli, V. *Mater. Chem.* **1982**, *7* (1), 89.
(64) Yanagisawa, Y.; Takaoka, K.; Yamabe, S.; Ito, T. *J. Phys. Chem.* **1995**, *99*, 3704.
(65) Mutch, G. A.; Morandi, S.; Walker, R.; Anderson, J. A.; Vega-Maza, D.; Operti, L.; Cerrato, G. *J. Phys. Chem. C* **2016**, *120*, 17570−17578.
(66) Mutch, G. A.; Anderson, J. A.; Walker, R.; Cerrato, G.; Morandi, S.; Operti, L.; Vega-Maza, D. *Int. J. Greenhouse Gas Control* **2016**, *51*, 126.
(67) Yu, F.; Phalak, N.; Sun, Z.; Fan, L. *Ind. Eng. Chem. Res.* **2012**, *51*, 2133.
(68) Zhang, K.; Li, X. S.; Chen, H.; Singh, P.; King, D. L. *J. Phys. Chem. C* **2016**, *120* (2), 1089.
(69) Zhang, K.; Li, X. S.; Li, W. Z.; Rohatgi, A.; Duan, Y.; Singh, P.; Li, L.; King, D. L. *Adv. Mater. Interfaces* **2014**, *1*, 1400030.
(70) Lee, C. H.; Lee, K. B. *Appl. Energy* **2017**, *205* (April), 316−322.
(71) Papaioannou, E. I.; Qi, H.; Metcalfe, I. S. *J. Membr. Sci.* **2015**, *485*, 87.
(72) Hammer, B.; Hansen, L. B.; Norskov, J. K. *Phys. Rev. B: Condens. Matter Mater. Phys.* **1999**, *59*, 7413.
(73) Perdew, J. P.; Burke, K.; Ernzerhof, M. *Phys. Rev. Lett.* **1996**, *77* (3), 3865.
(74) Kresse, G.; Furthmuller, J. *Phys. Rev. B: Condens. Matter Mater. Phys.* **1996**, *54* (16), 11169.
(75) Kresse, G.; Furthmuller, J. *Comput. Mater. Sci.* **1996**, *6*, 15.

DOI: 10.1021/jacs.8b01845
J. Am. Chem. Soc. 2018, 140, 4736−4742